Acta Biochim Biophys Sin xxxx, xx(x): xx-xx
https://cstr.cn/32197.14.abbs.2026061
https://doi.org/10.3724/abbs.2026061
Original Article

Original Article

Global O-GlcNAcome identifies O-GlcNAcylated proteins regulating oligodendrocyte precursor cell differentiation

Xinyue Jiang[1,†], Chi Zhang[1,†], Pingping Li[1,†], Ke Ye[1], Yixuan Song[1], and Mingliang Zhang[1,2,3,*]

[1]Department of Histoembryology, Genetics and Developmental Biology, Shanghai Key Laboratory of Reproductive Medicine, Shanghai Jiao Tong University School of Medicine, Shanghai 200025, China, [2]Department of Histology and Embryology, Zunyi Medical University, Zunyi 563000, China, and [3]School of Basic Medical Sciences, Ningxia Medical University, Yinchuan 750004, China
[†]These authors contributed equally to this work.
*Correspondence address. E-mail: mingliang.zhang@shsmu.edu.cn

Received 5 October 2025 Accepted 2 April 2026 Published 8 July 2026

Abstract

Oligodendrocyte precursor cells (OPCs) differentiate into myelinating oligodendrocytes to form the myelin sheaths essential for neural function, a process frequently compromised during aging and in diseases such as multiple sclerosis. However, the regulatory landscape of myelination remains incompletely understood. Here, we perform a comprehensive proteomic analysis of the O-GlcNAcome in postnatal day 0 mouse OPCs, identifying 165 O-GlcNAcylation sites across 118 proteins. These proteins are mostly nuclear and characterized by single-site modifications. Comparative analysis identifies 74 novel sites and 22 proteins uniquely O-GlcNAcylated in OPCs. Molecular docking suggests that O-GlcNAcylation might act as a dynamic regulator of OPC differentiation. Notably, global O-GlcNAcylation levels increase during the OPC-to-oligodendrocyte transition. By integrating our findings with multiple sclerosis-related transcriptomic and proteomic datasets, we identify candidate proteins linking O-GlcNAc dysregulation to demyelination. Among these, Vimentin exhibits a pronounced age-dependent discrepancy between decreased protein levels and elevated mRNA expression during differentiation. We validate threonines 35 and 63 as key O-GlcNAcylation sites on Vimentin. Functional assays confirm that blocking Vimentin O-GlcNAcylation enhances OPC differentiation. Collectively, our study establishes the first O-GlcNAc landscape for OPCs and suggests that O-GlcNAcylation is a pivotal regulator of OPC differentiation.

Key words oligodendrocyte precursor cell, O-GlcNAcylation, demyelinating disease, Vimentin, differentiation

Introduction

In the central nervous system (CNS), oligodendrocyte precursor cells (OPCs) differentiate into mature oligodendrocytes (OLs) to produce myelin sheaths. Myelin structures are essential for insulating neuronal axons, facilitating saltatory conduction, and providing metabolic support [1–4]. This developmental process represents a cornerstone of CNS plasticity and remyelination [5–8]. OPC differentiation depends on tightly coordinated gene expression, metabolic reprogramming, and cytoskeletal reorganization [9]. Consequently, dysregulation of this program could lead to severe pathologies, such as pediatric leukodystrophies and impaired myelin regeneration in adults [10]. In multiple sclerosis, a chronic autoimmune disorder characterized by demyelination, OPCs recruited to lesion sites often fail to differentiate into mature OLs, resulting in progressive axonal degeneration and disability [11–14]. Similarly, aging significantly reduces the regenerative capacity of OPCs, contributing to white matter loss and cognitive decline [15,16]. Despite substantial progress in OPC biology, the molecular and cellular drivers of differentiation remain incompletely understood. While certain remyelination regulators, such as muscarinic receptor pathways, are increasingly well defined [17], the post-translational modifications (PTMs) governing these processes are still largely unexplored.

The transition from OPCs to OLs is a metabolically intensive process that requires the coordination of the integration of cellular nutrient status with lineage progression [18]. A central mediator of

© The Author(s) 2026. This is an open access article distributed under the terms of the Creative Commons Attribution Non-Commercial License (https://creativecommons.org/licenses/by-nc/4.0/).

this nutrient sensing is O-linked β-N-acetylglucosaminylation (O-GlcNAcylation), a dynamic PTM involving the attachment of β-N-acetylglucosamine to serine or threonine residues. This modification is regulated by two primary enzymes, O-GlcNAc transferase (Ogt) and O-GlcNAcase (Oga) [19–21]. As a nutrient sensor, O-GlcNAcylation utilizes uridine diphosphate N-acetylglucosamine (UDP-GlcNAc) from the hexosamine biosynthetic pathway, converging glucose, amino acid, lipid, and nucleotide metabolism [22–24]. While this modification is abundant in the CNS and critical for neural development, synaptic function, and neurogenesis [25,26], its dysregulation is frequently linked to neurodegenerative conditions such as Alzheimer's and Parkinson's diseases [27–30]. In the context of multiple sclerosis, reduced GlcNAc levels have been correlated with disease progression, whereas supplementation has been shown to promote OL differentiation [31,32]. However, the specific O-GlcNAc-mediated mechanisms that drive OPC lineage progression remain to be elucidated.

Recent breakthroughs in mass spectrometry-based proteomics, supported by innovative chemical probes and chemoenzymatic labeling, have revolutionized the global characterization of the O-GlcNAcome [33]. Detailed mapping of these modifications has provided profound insights across various physiological contexts. For instance, landmark studies in murine synapses identified over 1750 sites on proteins involved in vesicle trafficking and cytoskeletal organization [34]. Quantitative approaches have further enabled precise mapping of O-GlcNAcylation dynamics [35]. Specifically, quantitative proteomics in post-mortem human Alzheimer's disease brain tissue utilizing chemoenzymatic photocleavage enrichment and TMT labelling, revealed 131 O-GlcNAcylated peptides with significant disease-associated changes [36]. Normalization to total protein abundance confirmed that these alterations reflected occupancy shifts rather than expression changes, with affected proteins enriched in synaptic pathways. In non-neural contexts, studies in mouse embryonic stem cells have demonstrated that elevated global O-GlcNAcylation is essential for maintaining pluripotency and must decrease to permit differentiation. This modification establishes a stemness-preserving network, as evidenced by the identification of 979 O-GlcNAcylated proteins that regulate the undifferentiated state [37]. These efforts have culminated in valuable resources, including the O-GlcNAcAtlas and the O-GlcNAc Database, which curate thousands of identified sites [38,39]. Despite this progress in mapping the general O-GlcNAcome, the O-GlcNAcylation landscape of OPCs and how it dynamically shifts during lineage progression remain unexplored.

In the present study, we characterized the O-GlcNAcome of postnatal day 0 (P0) mouse OPCs, mapped O-GlcNAcylated proteins and identified previously uncharacterized modification sites. These modified proteins are enriched in pathways related to cytoskeletal organization and neural development. By integrating our O-GlcNAcome dataset with transcriptomic and proteomic profiles from pathological (multiple sclerosis) and physiological (aging) contexts, we elucidated the dynamic changes in O-GlcNAcylated proteins across disease and aging. This analysis further pinpointed candidate regulators, including Vimentin (Vim), whose expression levels vary temporally in these conditions. Functional validation confirmed that O-GlcNAcylation of Vim is crucial for OPC differentiation. Together, these results provide the first O-GlcNAcome profile for OPCs, offering a potential therapeutic strategy for myelin regeneration.

Materials and Methods

Animals

All animal experiments were conducted in accordance with the guidelines approved by the Institutional Animal Care and Use Committee of Shanghai Jiao Tong University School of Medicine (approval No. JUMC2023-129-A). C57BL/6 mice (Lingchang Biotech, Shanghai, China) were housed in a specific-pathogen-free (SPF) facility under a controlled 12/12-h light/dark cycle, with *ad libitum* access to standard chow and water. Timed-pregnant females were used for the isolation of embryonic neural precursor cells, with the day of vaginal plug detection designated as embryonic day 0.5 (E0.5).

Brain tissue collection and processing for immunostaining

For the *in vivo* analysis of O-GlcNAcylation, P14, 2-month-old and 12-month-old mice were deeply anesthetized and transcardially perfused with ice-cold phosphate-buffered saline (PBS; pH 7.4) followed by 4% paraformaldehyde (PFA) in PBS for fixation. Brains were dissected, post-fixed in 4% PFA at 4°C overnight, and coronally sectioned at 30 μm using a vibrating microtome (Leica VT 1200 S, Wetzlar, Germany). Sections were then carefully transferred into 24-well plates containing PBS and stored at 4°C for immunostaining.

Primary neural progenitor cell isolation and culture

For *in vitro* differentiation and functional assays, primary neural progenitor cells (pNPCs) were isolated from the cerebral cortices of E12.5 C57BL/6J mouse embryos under sterile conditions in a laminar flow hood. Brains were dissected in ice-cold PBS, and cerebral hemispheres were separated. Meninges were removed using fine forceps, and cortices were minced and dissociated using Trpzyme (BasalMedia, Shanghai, China) for 15–20 min at 37°C. Digestion was stopped with 10% fetal bovine serum (FBS; LONSERA, Suzhou, China) in Dulbecco's modified Eagle's medium (DMEM; BasalMedia). The cell suspension was filtered through a 40-μm strainer, centrifuged at 200 *g* for 5 min, and resuspended in NPC culture medium consisting of Neurobasal medium (Gibco, Waltham, USA) and DMEM/F12 (Gibco) (1:1) supplemented with 1× N2 (Gibco), 1× B27 without VA (Gibco), 1× non-essential amino acids (NEAAs) (Gibco), 1× GlutaMAX (Gibco), 0.075% bovine serum albumin (BSA; YEASEN, Shanghai, China), 20 ng/mL mouse epidermal growth factor (mEGF; Peprotech, Rocky Hill, USA), 20 ng/mL basic fibroblast growth factor (bFGF; Peprotech), and 100 μg/mL penicillin-streptomycin (PS; BasalMedia). Cells were cultured as neurospheres in uncoated 10-cm dishes for suspension culture in a humidified incubator at 37°C with 5% CO_2, with partial medium replacement daily.

Neurospheres reaching ~200 μm in diameter were collected in a 50-mL centrifuge tube and allowed to settle for 3 min. The supernatant and unsettled cells were discarded, and 2 mL of pre-warmed Trpzyme (BasalMedia) was added to digest the neurospheres at 37°C for 5 min. Digestion was stopped with 10% FBS in DMEM, and the cells were centrifuged at 200 *g* for 3 min. The pellet was resuspended in 5 mL of pre-warmed NPC medium. Consequently, the cells were counted and seeded at 3×10^4 cells/cm^2 in Matrigel (Corning, New York, USA)-coated well plates and cultured

in fresh NPC medium at 37°C and 5% CO_2.

Differentiation of NPCs into oligodendrocyte precursor cells and oligodendrocytes

NPCs were seeded onto Matrigel-coated well plates at a density of 2.5×10^4 cells/cm^2 in OPC medium [DMEM/F12 basal medium supplemented with 1× N2, 1× B27 (without vitamin A), 1× GlutaMAX, 1× NEAA, 0.1 mM β-mercaptoethanol (Gibco), 200 ng/mL sonic hedgehog (shh; R&D Systems, Minneapolis, USA), 20 ng/mL bFGF, and 20 ng/mL platelet-derived growth factorAA (PDGF-AA; Peprotech). The cells were maintained in OPC medium for 3 days, with the medium refreshed every other day. OPC medium was then replaced with OL medium [DMEM/F12 supplemented with 1× N2, 1× B27 (without vitamin A), 1× GlutaMAX, 1× NEAA, 0.1 mM β-mercaptoethanol, 200 ng/mL Shh, 100 nM LDN193189, 100 ng/mL insulin-like growth factor 1 (IGF-1), 10 mM cyclic AMP, 10 ng/mL neurotrophin-3 (NT-3; Peprotech), and 40 ng/mL triiodothyronine (T3; MCE, Monmouth Junction, USA) for 4–5 days of culture, with half of the culture medium replaced every other day. During this process, the cells were maintained in an incubator at a constant temperature of 37°C with 5% CO_2.

Assessment of cell culture purity

To assess the purity of OPC and OL cultures derived from NPCs, cells were immunostained with lineage-specific markers. Purity was determined by calculating the percentage of platelet-derived growth factor receptor alpha (Pdgfrα)-positive cells (for OPCs) or myelin basic protein (Mbp)-positive cells (for OLs) relative to the total number of 4′,6-diamidino-2-phenylindole (DAPI)-stained nuclei. For primary OPCs isolated from P0 mice for proteomics, purity was assessed via flow cytometry using an anti-Pdgfrα antibody (Invitrogen, Carlsbad, USA). Cells were harvested and adjusted to a concentration of 1×10^6 cells/mL in ice-cold PBS containing 1% FBS. The cell suspension was incubated with the diluted APC-conjugated anti-Pdgfra antibody at 4°C for 30 min in the dark. After staining, cells were washed three times by centrifugation at 400 *g* for 5 min and resuspended in 500 μL of ice-cold PBS. Flow cytometry was performed using an Aria II cell sorter (BD Biosciences, Franklin Lakes, USA), and the data were analyzed with FlowJo 10.8.1 (https://www.flowjo.com/flowjo10/). The gating strategy was as follows: live cells were gated by side scatter area versus forward scatter area (SSC-A versus FSC-A), and singlets were subsequently selected by forward scatter height versus forward scatter area (FSC-H versus FSC-A). The purity of the isolated OPCs was determined by the percentage of the population positive for R660-APC-H signalsgated against an isotype control.

Functional analysis of O-GlcNAc cycling enzymes in NPCs

To investigate the effect of O-GlcNAc cycling on differentiation, primary NPCs were transfected with pcDNA3.1-Oga, pcDNA3.1-Ogt overexpression plasmids, or an empty vector control using the Neon Transfection System (Lingchang Biotech). Following transfection, cells were subjected to bleomycin selection for 3 days to enrich for transfected cells. The selected cells were then induced to differentiate into OPCs or mature OLs using the differentiation protocols described above. Differentiation efficiency was assessed by immunostaining for O4 and Mbp.

Culture of CG4 cells

CG4 cells were maintained in DMEM-F12 medium supplied with N2, B27, GlutaMAX, PDGF-AA and mEGF as described. Differentiation was induced by differentiation medium supplemented with B27, GlutaMAX, 50 mg/mL Transferrin (BasalMedia), 50 ng/mL ciliary neurotrophic factor (CNTF; MCE) and 40 ng/mL T3 for 3 days.

For the experiments on the effect of *Vim* on differentiation efficiency, CG4 cells were seeded on 12-well plates at a density of 1×10^5 cells per Matrigel-coated well and cultured for 1 day prior to transfection. The cells were then transfected with four different constructs, namely, the vector group, *Vim* KO + Vector group, *Vim* KO + *Vim*^{WT} group, and *Vim* KO + *Vim*$^{T35A\ T63A}$ group. After transfection, the cells were subjected to bleomycin selection for 3 days, followed by an additional 3 days of differentiation induction. Then, immunostaining was performed to determine the proportion of Mbp$^+$ cells.

Plasmid construction

Single guide RNAs (sgRNAs) were designed to target exon 1 of the mouse *Vim*, *Oga* and *Ogt* genes using the CRISPR design tool as described previously [40]. The selected sgRNA sequences for *Vim* (5′-GACACAGACCTGGTAGACA-3′ and 5′-CCCTTCGAAGCCATGTCTACC-3′), *Ogt* (5′-ACTGTCGGCCACGTTGCCCACGG-3′ and 5′-TAATAAGGCTGCAACCGGA-3′), and *Oga* (5′-TCAAGCGACGTTGGGGAGCGGG-3′ and 5′-GCGAGAGATGTATTCAGTGGAGG-3′) were cloned and inserted into a pX330-gRNA vector (Addgene, Watertown, USA) that co-expressed Cas9 nuclease and an mCherry reporter. The full-length coding sequence of mouse *Vim* (NM_011701.4) was amplified using polymerase chain reaction (PCR) from the total RNA extracted from mouse brains. The PCR products were then cloned and inserted into a pcDNA3.1 vector (Addgene). To generate constructs for Oga and Ogt overexpression, the full-length coding sequences of mouse *Oga* (*Mgea5*, NM_023799) and *Ogt* (NM_139144) were amplified from mouse brain cDNA using PCR and cloned and inserted into the pcDNA3.1 vector.

To generate constructs for immunoprecipitation (IP) assays, we constructed the pcDNA3.1-Flag-Vim-HA plasmid. The full-length coding sequence of mouse *Vim* (NM_011701.4) was amplified with an N-terminal Flag tag and a C-terminal HA tag and subsequently cloned and inserted into the pcDNA3.1 vector. Site-directed mutagenesis was performed on this template to generate the O-GlcNAc-deficient mutant pcDNA3.1-Flag-Vim$^{T35A\ T63A}$-HA, in which threonine 35 and threonine 63 were substituted with alanine.

Cell transfection

Human embryonic kidney (HEK) 293T cells (ATCC, Manassas, USA) were maintained in DMEM supplemented with 10% FBS. For cell transfection, HEK293T cells were seeded at a density of 5×10^5 cells per well in 6-well plates. At ~70%–80% confluence, cells were transfected with 3 μg plasmid DNA per well using polyethylenimine (PEI; Polysciences, Warrington, USA). NPCs were transfected using the Neon Transfection System (Invitrogen) according to the manufacturer's instructions.

Protein sample preparation

For the O-GlcNAcome analysis, primary OPCs were isolated from a pool of 100 P0 neonatal mice. The brains were rapidly dissected,

and the brainstem, cerebellum, and midbrain were removed. The remaining tissue was digested using Trpzyme to create a single-cell suspension. OPCs were then purified from this suspension using the CD140α (Pdgfrα) MicroBead Kit (Miltenyi Biotec, Cologne, Germany) according to the manufacturer's protocol. Total protein was extracted from OPCs using lysis buffer containing 8 M urea and 1% protease inhibitor cocktail, sonicated three times on ice with a high-intensity ultrasonic processor (Scientz, Ningbo, China) in lysis buffer, and centrifuged at 12,000 *g* and 4°C for 10 min. The supernatant was collected, and the protein concentration was determined using a BCA kit (Yeasen Biotechnology, Shanghai, China) according to the manufacturer's instructions.

Liquid chromatography-tandem mass spectrometry (LC-MS/MS)

O-GlcNAcome profiling was performed as a commercial service by PTM Bio (Hangzhou, China). To concentrate the proteins and remove interfering substances, acetone precipitation was performed. Briefly, one volume of pre-cooled acetone was added to the sample and vortexed, followed by the addition of four additional volumes of pre-cooled acetone. The mixture was incubated at −20° C for 2 h. The resulting protein precipitates were collected by centrifugation at 4500 *g* for 5 min at 4°C. The supernatant was discarded, and the pellet was washed twice with pre-cooled acetone. Proteins were resuspended in digestion buffer and subjected to primary digestion with trypsin (1:50 trypsin-to-protein w/w ratio) overnight at 37°C. Subsequently, the sample was reduced with 5 mM dithiothreitol (DTT) for 60 min at 56°C and alkylated with 11 mM iodoacetamide (IAA) for 45 min at room temperature in the dark. A secondary digestion was then performed with trypsin (1:100 w/w) for 4 h at 37°C to ensure complete enzymatic cleavage.

Peptides were desalted using a C18 SPE column (activated with methanol and equilibrated with 0.1% TFA). Peptides were eluted with 80% acetonitrile (ACN) and quantified using a BCA assay. For the enrichment of O-GlcNAc-modified peptides, desalted peptides were redissolved in NETN buffer (100 mM NaCl, 1 mM EDTA, 50 mM Tris-HCl, and 0.5% NP-40, pH 8.0) and incubated with O-GlcNAc antibody-conjugated beads (PTM-954; PTM Bio) at 4°C overnight with gentle rotation. The immunocomplexes were washed four times with NETN buffer and twice with double-distilled water. The enriched glycopeptides were eluted and subjected to a final cleanup using C18 ZipTips to remove trace salts prior to LC-MS/MS analysis.

The tryptic peptides were dissolved in solvent A (0.1% formic acid, 2% acetonitrile in water) and directly loaded onto a custom-made reversed-phase analytical column (25 cm length, 75/100 μm i.d.). Peptides were separated with a gradient from 6% to 24% solvent B (0.1% formic acid in acetonitrile) over 70 min, 24% to 35% in 14 min and climbing to 80% in 3 min and then holding at 80% for the last 3 min, all at a constant flow rate of 450 nL/min on a nanoElute UHPLC system (Bruker Daltonics, Bremen, Germany). The peptides were subjected to capillary source followed by timsTOF Pro (Bruker Daltonics) mass spectrometry. The electrospray voltage was set to 1.60 kV. Precursors and fragments were analyzed at the TOF detector, with an MS/MS scan range from 100 to 1700 m/z. The timsTOF Pro was operated in parallel accumulation serial fragmentation (PASEF) mode. Precursors with charge states of 0 to 5 were selected for fragmentation, and 10 PASEF-MS/MS scans were acquired per cycle. The dynamic exclusion was set to 30 s.

The raw MS/MS data were processed using the MaxQuant search engine (v1.6.15.0). Tandem mass spectra were searched against the Mus_musculus_10090_SP_20210721.fasta database concatenated with a reverse decoy database. Trypsin/P was specified as the cleavage enzyme allowing up to 2 missing cleavages. The mass tolerance for precursor ions was set to 20 ppm for both the first and main searches, and the fragment ion mass tolerance was 20 ppm. Carbamidomethylation on Cys was set as a fixed modification. Acetylation (protein N-terminal), oxidation (Met), and O-glycosylation (+203.08 Da on Ser/Thr) were specified as variable modifications. The false discovery rates (FDRs) of proteins, peptides and PSMs were adjusted to < 1%.

Western blot analysis

Cells were lysed in RIPA buffer (Beyotime, Shanghai, China) supplemented with phenylmethanesulfonyl fluoride (PMSF; Beyotime) and Thiamet-G (APExBIO, Houston, USA), homogenized for 30 min on ice and centrifuged at 17,000 *g* for 30 min. Protein samples (10 mg) were separated using 10% sodium dodecyl sulfate-polyacrylamide gel electrophoresis (SDS-PAGE) gels and transferred to polyvinylidene fluoride (PVDF; Millipore, Billerica, USA) membranes. Membranes were blocked in 5% skim milk at room temperature for 1 h and then incubated with primary antibodies against O-GlcNAc (Invitrogen) and β-actin (ABclonal, Wuhan, China) (1:1000 dilution) at 4°C overnight. Membranes were consequently washed using TBST three times and then incubated with the appropriate HRP-conjugated secondary antibodies (ABclonal) at room temperature for 1 h. Bands were visualized using a luminescent image analyzer (GE Imagination LAS 4000; GE Imagination, Boston, USA). The protein band intensity was quantified with ImageJ (NIH, Bethesda, USA) software.

Immunoprecipitation

Cells expressing Flag-HA-tagged Vim^{WT} and $Vim^{T35A\ T63A}$ were lysed in IP lysis buffer containing protease inhibitors and Thiamet-G. Lysates were incubated with anti-Flag magnetic beads (Bimake, Houston, USA) overnight at 4°C with rotation. The beads were washed extensively with lysis buffer, and the bound protein complexes were eluted by boiling in SDS loading buffer. The eluates were subsequently analyzed by western blot analysis using anti-O-GlcNAc (1:1000; PTM Bio), anti-Flag (1:10,000; Sigma-Aldrich, Melbourne, Australia) and anti-HA (1:10,000; ABclonal) antibodies to evaluate the O-GlcNAcylation levels of Vim.

Quantitative real-time PCR (qRT-PCR)

Total RNA was extracted from cultured NPCs, OPCs, and OLs at various stages of differentiation using TRNzol Universal Reagent (TIANGEN, Beijing, China) according to the manufacturer's protocol. Briefly, cells were lysed directly in a culture dish, and RNA was isolated following extraction using chloroform and precipitation using isopropanol. The RNA pellet was washed with 75% ethanol, air-dried, and resuspended in RNase-free water. The quantity and purity of the RNA were assessed using a NanoDrop 2000 spectrophotometer (Thermo Fisher Scientific, Waltham, USA); samples having an A260/280 ratio between 1.8 and 2.0 were used for downstream applications.

First-strand cDNA was synthesized from 1 μg DNase-treated total

RNA using a HiScript II1st Strand cDNA Synthesis kit (Vazyme, Nanjing, China), which included a blend of oligo(dT) and random hexamer primers to ensure unbiased representation of the transcriptome.

qRT-PCR was performed on a CFX96 Real-Time PCR Detection System (Bio-Rad, Hercules, USA) using ChamQ SYBR Color qRT-PCR Master Mix (Vazyme). Each 10 μL reaction mixture contained 5 μL 2× ChamQ SYBR qRT-PCR Master Mix, 200 nM each forward and reverse primer, and 1 μL diluted cDNA template. Thermal cycling conditions were as follows: initial denaturation at 95°C for 3 min, followed by 40 cycles at 95°C for 15 s and at 60°C for 60 s. A melt curve analysis was performed at the end of each run to verify the specificity of the amplification product. Gene expression levels were quantified using the comparative Ct ($2^{-\Delta\Delta Ct}$) method with expression normalized to that of the housekeeping gene *β-actin* (*Actb*). The primer sequences used for qRT-PCR are listed in Table 1.

Immunostaining and imaging

OLs and HEK293T cells were fixed with 4% PFA in PBS for 10 min at room temperature, washed three times with PBS, permeabilized with 0.2% Triton X-100 in PBS for 10 min, and blocked with 7.5% BSA in PBS for 1 h. Cells were incubated overnight at 4°C with primary antibodies against O-GlcNAc (1:500; Abcam, Cambridge, UK), O4 (1:500; R&D Systems, Minneapolis, USA), Pdgfrα (1:500; Oasis, Hangzhou, China), or HA (1:500; ABclonal) in blocking buffer, followed by Alexa Fluor-conjugated secondary antibodies (1:1000; Invitrogen) and DAPI for 1 h at room temperature. Tissue sections were blocked with 5% donkey serum in PBS with 0.1% Triton X-100 for 1 h, incubated with primary antibodies against O-GlcNAc (1:500; Abcam), CC1 (1:500; Oasis), or Pdgfrα (1:500; Oasis) overnight at 4°C, and then with secondary antibodies for 2 h. Imaging was performed using a Nikon ECLIPSE Ti2 (Nikon, Melville, USA).

Cell proliferation and apoptosis assays

To assess cell proliferation, transfected CG4 cells were fixed with 4% PFA and subjected to immunofluorescence staining. Cells were incubated with primary antibodies against Ki67 (1:500; MCE) and Sox10 (1:500; Oasis) overnight at 4°C, followed by incubation with the corresponding secondary antibodies. The proliferation rate was quantified as the percentage of $Ki67^+$ cells within the $Sox10^+$ cell population.

For the assessment of apoptosis, the Terminal Deoxynucleotidyl Transferase dUTP Nick End Labeling (TUNEL) assay was performed using a TUNEL BrightGreen Apoptosis Detection kit (Vazyme) according to the manufacturer's instructions. Cells were simultaneously co-stained with an anti-Pdgfrα antibody (1:500; Oasis) to identify OPCs. The apoptotic rate was calculated as the ratio of $TUNEL^+Pdgfr\alpha^+$ cells to the total $Pdgfr\alpha^+$ population. Images were acquired and analyzed using the same microscopy and software settings as described above.

Image quantification

All fluorescence images were analyzed using ImageJ. To ensure accurate interpretation of the O-GlcNAc signal in OPCs and oligodendrocytes, we measured the mean fluorescence intensity (MFI) exclusively in cells positively identified by lineage-specific markers (Pdgfrα for OPCs; O4 for OLs; CC1 for more mature oligodendrocytes; and Mbp for functional oligodendrocytes). This per-cell analysis eliminates the need for physical isolation and avoids potential confounding signals from non-lineage cells. Specifically, individual marker-positive cells were segmented based on their immunostaining, and O-GlcNAc MFI was quantified strictly within these cellular boundaries.

Proteomics data analysis and functional annotation

Gene Ontology (GO) and Kyoto Encyclopedia of Genes and Genomes (KEGG) pathway analyses were performed using DAVID [41]. Bubble plots were generated using an online platform (https://www.bioinformatics.com.cn, accessed December 10, 2024) [42]. Protein localization was predicted using WoLF PSORT [43].

For the analysis of O-GlcNAcylation motifs, 21 amino acid sequences (± 10 residues) flanking identified sites were analyzed using OmicShare tools [44]. Intrinsically disordered regions and linear interacting peptides were identified using MobiDB [45], and protein domains were annotated using the Pfam database [46].

Protein-protein interaction (PPI) network analysis

The list of O-GlcNAcylated proteins was submitted to STRING (https://string-db.org) to extract known and predicted functional associations (confidence score of > 0.4) and the results were visualized using Cytoscape (V3.10.1).

Molecular docking simulations

Molecular docking was performed using HPEPDOCK [47] with the human OGT crystal structure (PDB ID: 4GYW) as the receptor [48,49]. Structures were prepared in PyMOL (v3.1.1) by removing water molecules, adding polar hydrogens, and assigning Gasteiger

Table 1. Sequences of primers used for qRT-PCR analysis

Gene	Forward primer (5′→3′)	Reverse primer (5′→3′)
Vim	CGTCCACACGCACCTACAG	GGGGGATGAGGAATAGAGGCT
Actb	GGTCATCACTATTGGCAACGAGC	CCAGACAGCACTGTGTTGGCATA
Dbn1	GCTTGCAGCGTCAGGAGAA	TCCTCACCAACCCAGTTGATG
Flnb	GACCACGAAAGCATTAAGCTCG	CTGAATCCATCCCAGTAGCCT
Mbp	TCCATCCCAAGGAAAGGGGA	TCTGCCTCCGTAGCCAAATC
Plp1	CTGCAAAACAGCCGAGTTCC	ATCAGAACTTGGTGCCTCGG
Mog	CCTTCAGGCTTCTTGGGGTA	TCACTCTGAACTGTCCTGCG
Mag	GCCAGACCATCCAACCTTCT	CCTCACCTCAGTCTCCCTGA
Pdgfrα	AGAGTTACACGTTTGAGCTGTC	GTCCCTCCACGGTACTCCT
Olig2	GGGAGGTCATGCCTTACGC	CTCCAGCGAGTTGGTGAGC

charges. The interface areas and ΔiG between OGT and the peptides were calculated using PDBePISA (https://www.ebi.ac.uk/pdbe/pisa/).

Statistical analysis

Data are presented as the mean ± SD from at least three independent experiments. Statistical analyses were performed using GraphPad Prism 9 (GraphPad Software, San Diego, USA). We explicitly define that for all assays, "*n*" represents the number of independent biological replicates. In brief, for *in vitro* cell culture assays, "*n*" indicates the number of independent experiments, each with three technical replicates; for *in vivo* experiments, "*n*" denotes the number of mice per group, with samples collected from individual mice processed as separate biological replicates. Comparisons between two groups were performed using a two-tailed unpaired Student's *t* test. Multiple-group comparisons were performed using one-way ANOVA with Tukey's *post hoc* test as appropriate. Specific statistical tests used are clearly stated in each figure legend. No statistical methods were used to predetermine the sample size.

Results

Global O-GlcNAcylation levels in OPCs

To investigate the role of O-GlcNAcylation in OPC lineage progression, we first characterized global O-GlcNAc levels during the transition from OPCs to mature OLs. To this end, primary NPCs isolated from E12.5 mouse cortices were cultured under established differentiation conditions (Supplementary Figure S1A,B). Immunofluorescence showed approximately 20% Pdgfrα$^+$ OPCs at the precursor stage and 12% Mbp$^+$ OLs following differentiation (Supplementary Figure S1C,D). Both immunostaining and western blot analyses revealed an upregulation of global O-GlcNAcylation in OLs relative to OPCs (Figure 1A–D). Quantitative analysis of *in vitro* cultures showed that the O-GlcNAc MFI was higher in O4$^+$ OLs (45.4) than in Pdgfrα$^+$ OPCs (5.2) (Figure 1A,B). This protein-level increase was further confirmed by western blot analysis, which exhibited a 1.3-fold increase in global O-GlcNAcylation during differentiation (Figure 1C,D). Consistent with these changes, qRT-PCR analysis demonstrated a 1.2-fold induction of *Ogt* mRNA as cells transitioned from the precursor stage to mature OLs (Figure 1E).

To validate these findings *in vivo*, we performed immunostaining on brain sections from P14 and 2-month-old (2 M) adult mice, focusing on the corpus callosum (CC) and cortex (Figure 1F,I). Consistent with our *in vitro* data, O-GlcNAc levels at P14 were lower in Pdgfrα$^+$ OPCs (18.6) than in CC1$^+$ OLs (23.6) within the cortex, while in the CC, the intensity increased from 14.8 in OPCs to 20.1 in OLs (Figure 1G,H). A similar trend was observed in the 2 M adult brain, with MFI rising from 20.4 in OPCs to 29.4 in OLs in the cortex and from 17.9 to 28.0 in the CC (Figure 1J,K). Density plots of MFI revealed a consistent shift in the distribution curve for OLs compared to OPCs across both ages and regions (Figure 1G,H,J,K).

To determine the functional requirement for O-GlcNAc cycling in lineage progression, we genetically modulated the expression of O-GlcNAc cycling enzymes in primary E12.5 NPCs. Primary NPCs were transfected with plasmids for either the overexpression or CRISPR/Cas9-mediated knockout of *Ogt* or *Oga*, followed by bleomycin selection and differentiation. Immunostaining analysis revealed that decreasing global O-GlcNAcylation, achieved through either Oga overexpression or *Ogt* knockout, impaired the transition from OPCs to OLs (Supplementary Figure S2A,D). Specifically, Oga overexpression reduced the proportion of O4$^+$ OLs from approximately 7% in control cultures to approximately 2%, while Mbp$^+$ cells decreased from approximately 4% to 1% (Supplementary Figure S2B,C). Mirroring these results, *Ogt* knockout similarly impaired the transition, with O4$^+$ and Mbp$^+$ percentages dropping to 1.8% and 0.5%, respectively (Supplementary Figure S2E,F). Conversely, augmenting O-GlcNAc levels via *Ogt* overexpression or *Oga* knockout facilitated the differentiation process. Overexpression of *Ogt* promoted maturation, increasing the percentage of O4$^+$ cells to approximately 10% and Mbp$^+$ cells to approximately 6% compared to empty vector controls (Supplementary Figure S2B, C). Furthermore, *Oga* knockout led to an increase in O4$^+$ and Mbp$^+$ populations to 7% and 5.5%, respectively (Supplementary Figure S2E,F). Collectively, these results demonstrate that O-GlcNAcylation is critical for OPC differentiation.

Proteomic profiling of O-GlcNAcome in OPCs

To comprehensively characterize the O-GlcNAc landscape in OPCs, we conducted a proteomic analysis. Primary OPCs were isolated from P0 mouse brains, followed by the enrichment of O-GlcNAcylated proteins using a combinatorial approach involving O-GlcNAc-specific antibody-conjugated beads and metal affinity chromatography (Figure 2A). The high purity of the isolated primary OPCs, determined to be 91.8% via flow cytometry, ensured the reliability and fidelity of the downstream proteomic dataset (Supplementary Figure S3). Enriched O-GlcNAcylated peptides were analyzed using LC-MS/MS. This analysis processed 15,932 total spectra, yielding 3683 matched spectra and 3065 peptides, which ultimately identified 165 O-GlcNAcylation sites mapping to 118 distinct proteins (Figure 2B). Subcellular localization analysis revealed that the OPC O-GlcNAcome was predominantly nuclear (64.4%), with substantial representation in the cytoplasm (15.3%) and mitochondria (4.3%) (Figure 2C). Notably, 78.8% of the identified proteins harbored a single O-GlcNAcylation site, while 21.2% contained two or more sites (Figure 2D). We cross-referenced our dataset with the O-GlcNAc Database and O-GlcNAcAtlas (v3.0) [38,39]. This comparative analysis identified 74 novel O-GlcNAcylation sites (44.8%) on 67 proteins (56.8%) within our OPC dataset. Strikingly, 22 of these proteins had not been previously reported to undergo O-GlcNAcylation in any biological context (Figure 2E,F).

Functional annotation of the OPC O-GlcNAcome

We performed a functional enrichment analysis of O-GlcNAcylated proteins in OPCs. GO analysis revealed a significant enrichment of these proteins in biological processes essential for OPC lineage progression (Figure 3A). Cellular component analysis indicated that the O-GlcNAcome is primarily localized to the cell body and cytoplasm (Figure 3B). Molecular function categories were enriched in protein binding and protein domain-specific binding (Figure 3C). KEGG pathway analysis further revealed that these O-GlcNAcylated proteins are involved in gap junction signaling. Additionally, several neurodegenerative pathways were enriched, including those associated with Alzheimer's, Parkinson's, and Huntington's diseases (Figure 3D). To investigate the topological organization of these modified proteins, we constructed a PPI network. This analysis identified several nodes, including Actb, Mapt, Tubb3, Htt, Ywhaq, and Srcin1 (Figure 3E). These proteins were reported to coordinate cytoskeletal dynamics and intracellular transport, both

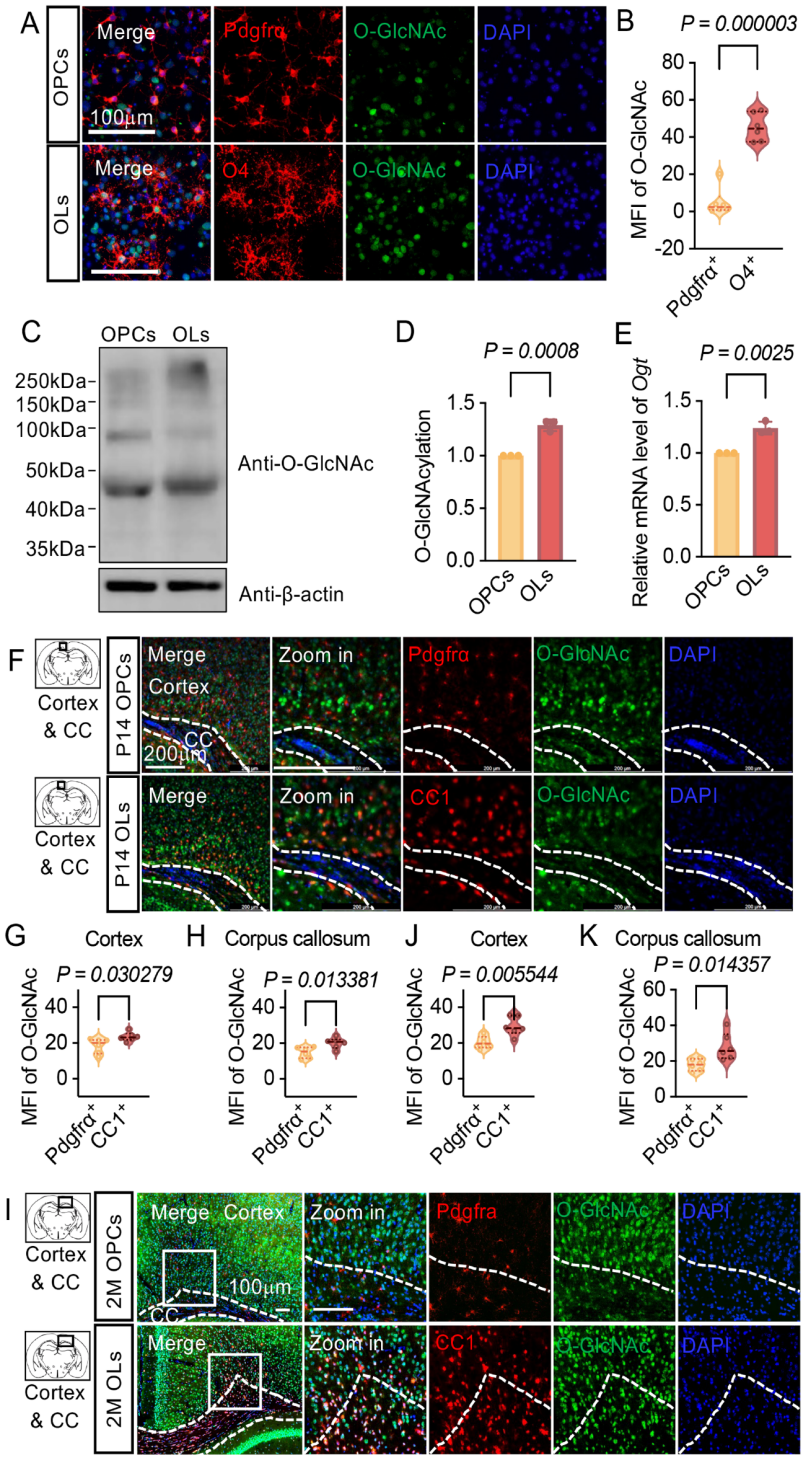


Figure 1. O-GlcNAcylation levels in the oligodendrocyte lineage (A) Representative immunostaining images of OPCs (Pdgfrα+, red) and differentiating OLs (O4+, red) differentiated from primary NPCs. Staining shows O-GlcNAcylation (O-GlcNAc+, green) and nuclei (DAPI, blue). Scale bar: 100 μm. *n* = 6 independent biological experiments. (B) Quantification of the mean fluorescence intensity (MFI) of O-GlcNAc in Pdgfrα+ OPCs and O4+ OLs from (A). (C,D) Western blots (C) and quantification (D) of total O-GlcNAcylation levels in OPCs and OLs. *n* = 3 independent biological experiments. (E) qRT-PCR analysis of O-GlcNAc transferase (*Ogt*) mRNA expression in OPCs and OLs. (F) *In vivo* immunolabeling of OPCs (Pdgfrα+, red) and mature OLs (CC1+, red) in the brains of P14 mice, showing O-GlcNAcylation levels (O-GlcNAc+, green). Scale bar: 200 μm. *n* = 6 mice per group. (G,H) Quantification of the MFI of O-GlcNAc in *in vivo* Pdgfrα+ OPCs and CC1+ OLs in the cortex (G) and corpus callosum (CC) (H). (I–K) *In vivo* immunostaining images (I) and quantification (J,K) of O-GlcNAcylation levels in Pdgfrα+ OPCs and CC1+ OLs in the 2-month-old (2 M) mouse brain. Scale bar: 100 μm. *n* = 6 mice per group. All quantifications were performed on a per cell basis. *P* values were calculated using two-tailed unpaired Student's *t* test.

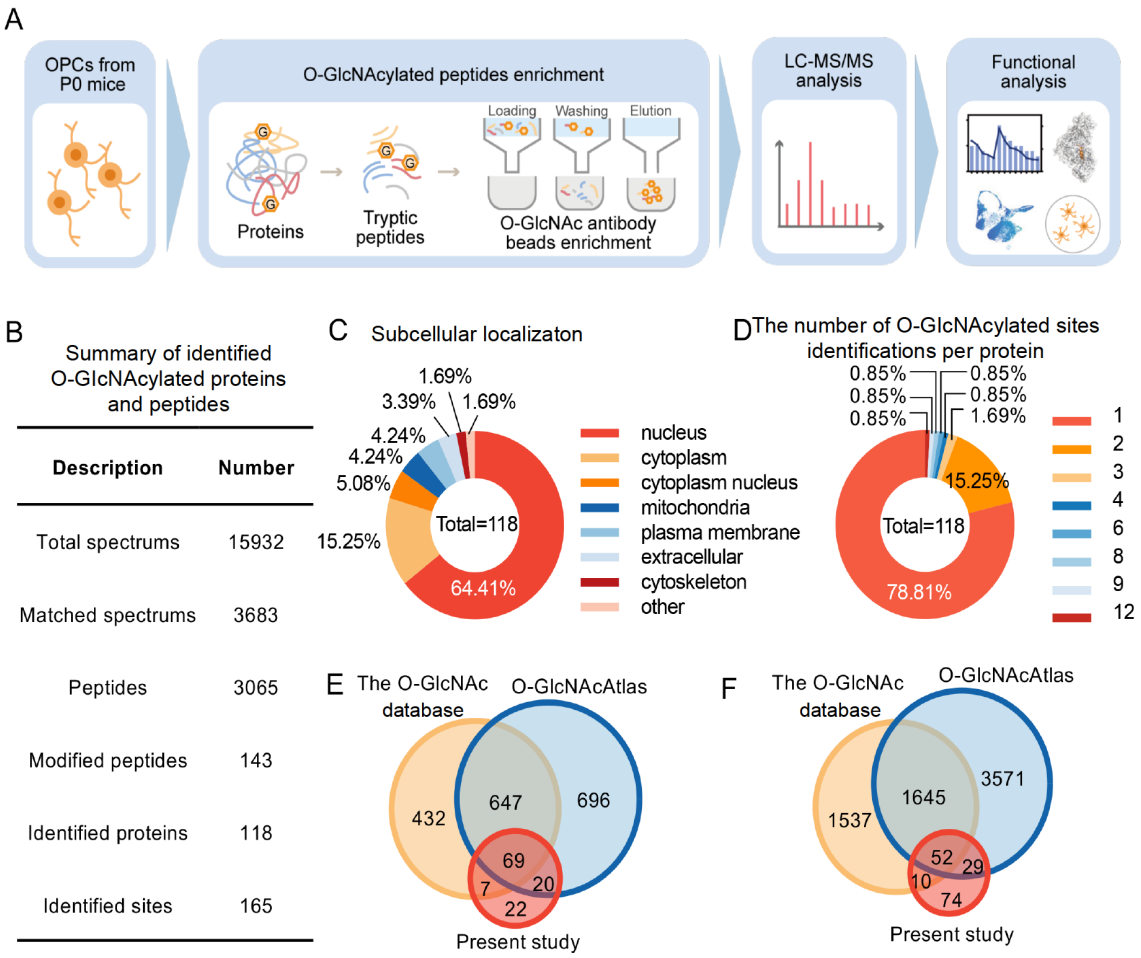


Figure 2. Proteomic analysis of O-GlcNAcylated proteins in OPCs (A) Schematic of the experimental workflow for identifying O-GlcNAcylated proteins in OPCs, including OPC isolation from P0 mouse brains, protein extraction, O-GlcNAcylated peptide enrichment, LC-MS/MS analysis, and functional analysis. (B) Summary of the proteomics results, detailing the number of total spectra, matched spectra, peptides, modified peptides, identified proteins, and sites. (C) Pie chart showing the subcellular localization of the 118 identified O-GlcNAcylated proteins. (D) Distribution of O-GlcNAcylated sites per protein. (E,F) Venn diagrams comparing the identified O-GlcNAcylated proteins (E) and sites (F) from this study with the O-GlcNAc Database and O-GlcNAcAtlas, revealing 22 novel O-GlcNAcylated proteins and 74 novel modification sites.

of which are essential processes underpinning the migration and differentiation of OPCs [9,50–54]. Collectively, these findings provide a functional framework for the OPC O-GlcNAcome.

Motif and structural analysis of OPC O-GlcNAcylated proteins

To characterize the sequence and structural determinants underlying O-GlcNAcylation in OPCs, we conducted a motif analysis on the 165 identified O-GlcNAcylation sites. This analysis revealed a distinct preference for proline at the –3 and –2 positions, valine at the –1 position relative to the modified residue, and arginine at the +1 position, with serine and alanine enriched in the flanking regions (Figure 4A). These features are consistent with the known structural roles of proline in imparting conformational rigidity and stabilizing binding pockets, while distal arginine residues may facilitate downstream PPIs [55,56]. Previous studies have established that Ogt modification sites are predominantly localized within intrinsically disordered regions (IDRs) [34,57], which is essential for dynamic PPIs, molecular recognition, and cellular signaling regulation [58]. We further integrated structural predictions from MobiDB, covering IDRs and linear interacting peptides (LIPs), and Pfam for structured domains to contextualize these modification sites. Of the 165 O-GlcNAcylation sites identified, the majority (69.7%, $n = 115$) were localized within IDRs, while 35.2% ($n = 58$) were situated within LIPs. In contrast, only a minority (19.4%, $n = 32$) of sites mapped to ordered domains (Figure 4B–D). Functional enrichment analysis revealed distinct biological roles based on structural context. Proteins modified within IDRs showed strong enrichment in synapse organization and regulation of protein-containing complex assembly (Figure 4B). Proteins modified at LIP sites were linked to synapse organization, negative regulation of the vascular endothelial growth factor signaling pathway and the epidermal growth factor receptor signaling pathway (Figure 4C). The limited number of sites within structured domains was associated with

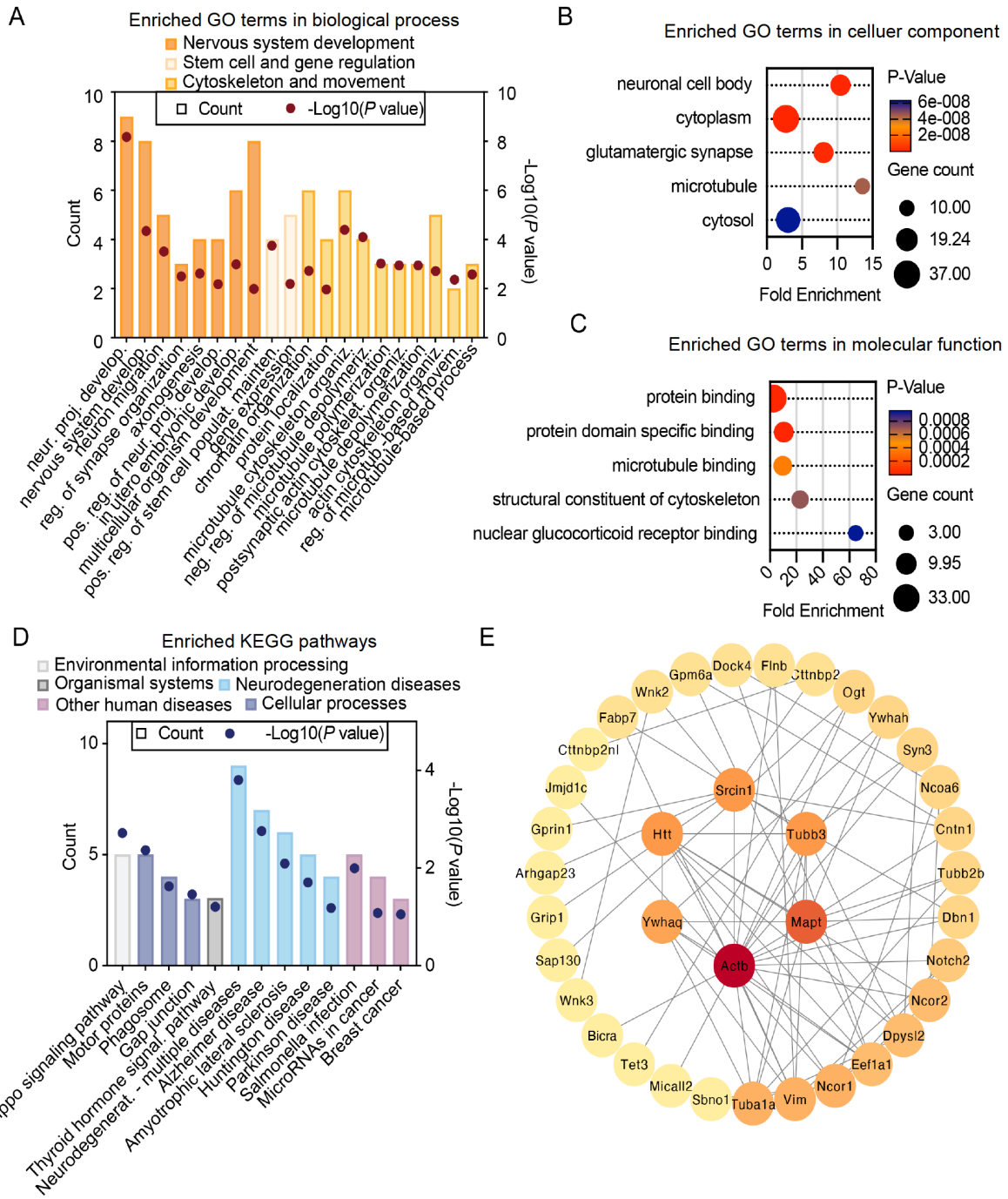


Figure 3. Functional annotation of OPC O-GlcNAcylated proteins (A) GO enrichment analysis of OPC O-GlcNAcylated proteins. (B,C) Bubble chart of enriched GO terms in cellular component (B) and molecular function (C) for O-GlcNAcylated proteins. (D) KEGG pathway analysis reveals associations with pathways linked to neurodegenerative diseases, including Alzheimer's disease. (E) PPI network of the OPC-specific O-GlcNAcylated proteins.

cytoskeletal regulation (Figure 4D).

To highlight the unique regulatory profile of the oligodendrocyte lineage, we performed a parallel analysis focusing exclusively on the 74 newly identified O-GlcNAcylation sites (Supplementary Figure S4A,C–E). Remarkably, the structural distribution of these sites showed a similar preference, with a predominant localization in IDRs (64.9%) and LIPs (35.1%). However, these OPC-specific modifications were more specifically enriched in pathways essential for CNS development and cytoskeletal organization.

Chemical properties of O-GlcNAcylation motifs in OPCs

To characterize the chemical microenvironment governing Ogt

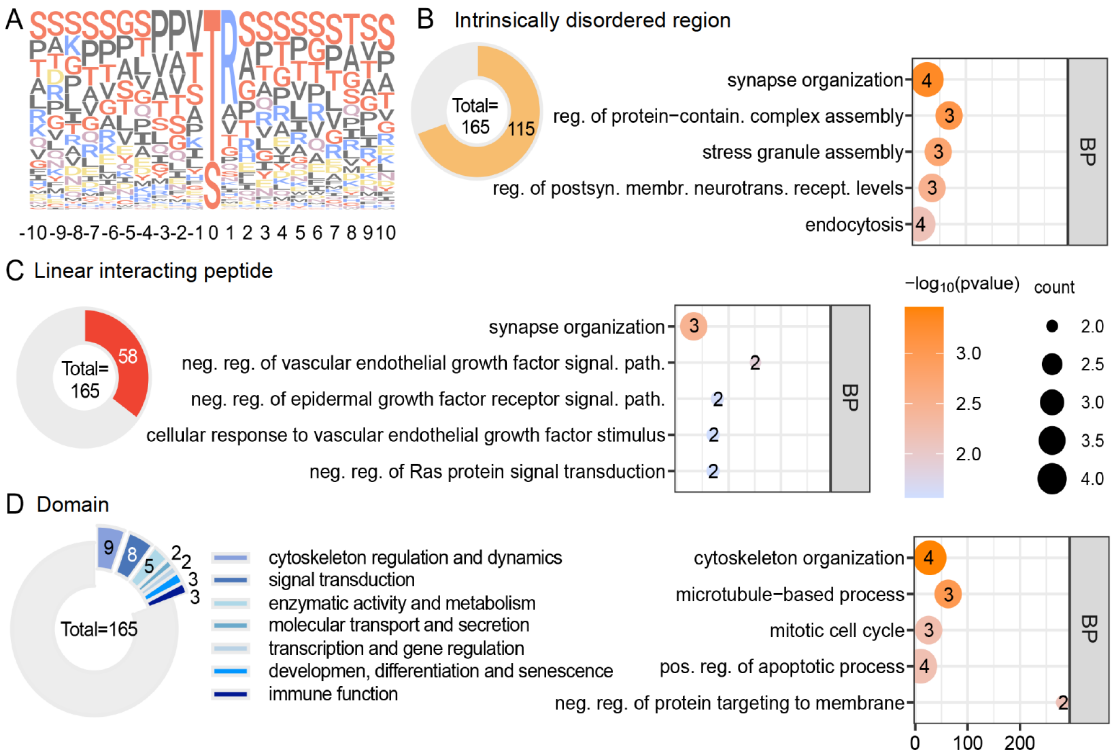


Figure 4. Motif and structural analysis of OPC O-GlcNAcylated sites (A) Motif analysis of the amino acid sequences surrounding the OPC O-GlcNAcylated sites. (B) Distribution of O-GlcNAcylated sites within intrinsically disordered regions (IDRs) and GO enrichment analysis of the corresponding proteins. (C) Distribution of O-GlcNAcylated sites within linear interaction peptides (LIPs) and GO enrichment analysis of the corresponding proteins. (D) Distribution of O-GlcNAcylated sites within structured protein domains and the functional classification of the corresponding proteins.

substrate recognition, we analyzed the amino acid residues flanking the 165 identified O-GlcNAcylation sites (Figure 5A). Small, nonpolar, and hydrophobic residues prevailed in the immediate vicinity, specifically from positions −3 to +3, while basic residues were enriched at the +1 position. Notably, the 74 novel O-GlcNAcylation sites exhibited identical chemical preferences to the global profile (Supplementary Figure S4B). This prevalence of hydrophobic residues suggests that O-GlcNAcylation frequently occurs at protein-protein interfaces, potentially modulating interaction specificity and complex stability [59]. Furthermore, the presence of specific polar and ionizable residues likely facilitates the stabilization of the Ogt-substrate complex through polar-polar contacts within these hydrophobic pockets [56].

To evaluate the energetic landscape of Ogt binding, we performed molecular docking simulations using representative O-GlcNAcylated peptides from OPCs, synapses, and HeLa cells [34,35]. These simulations revealed that OPC-derived peptides exhibit intermediate binding free energies (ΔG) compared to their synaptic and HeLa-derived counterparts (Figure 5B,C). Such intermediate energetics may allow for reversible and dynamic modulation of the O-GlcNAcome in response to fluctuating metabolic cues throughout the oligodendrocyte lineage.

Association of OPC O-GlcNAcylated proteins with multiple sclerosis

To further investigate the potential involvement of O-GlcNAcylated proteins in demyelinating pathologies, we intersected these O-GlcNAc-modified proteins with two multiple sclerosis-related resources: a single-nucleus RNA sequencing (snRNA-seq) dataset, from which we computationally isolated the OPC cluster, and a proteomic dataset derived from multiple sclerosis lesions [60,61]. This integrative analysis identified 15 O-GlcNAcylated proteins shared across all datasets (Table 2 and Supplementary Figure S5A). These genes are enriched in biological processes related to cytoskeleton organization (Supplementary Figure S5B). Subcellularly, these proteins were predominantly localized to the cytoplasm and cell projection (Supplementary Figure S5C). Molecular function analysis further indicated a strong enrichment in profilin binding (Supplementary Figure S5D). KEGG pathway analysis revealed that these O-GlcNAcylated candidates are significantly enriched in four functional pathways: IgSF CAM signaling, microRNAs in cancer, Alzheimer's disease, and pathways of neurodegeneration (Supplementary Figure S5E).

Among the overlapping candidates, *Vim*, *Dbn1*, and *Flnb* exhibited the most pronounced expression changes ($|\log_2 FC| > 1.5$ in at least one dataset) in people with multiple sclerosis (Supplementary Figure S5F). Therefore, we focused our study on these candidates.

Expression dynamics of OPC O-GlcNAcylated proteins during aging

To investigate the potential role of O-GlcNAcylation in the context of aging, we first measured total O-GlcNAc levels in Pdgfrα$^+$ OPCs in mouse brains at P14, 2 months (2 M), and 12 M (Supplementary

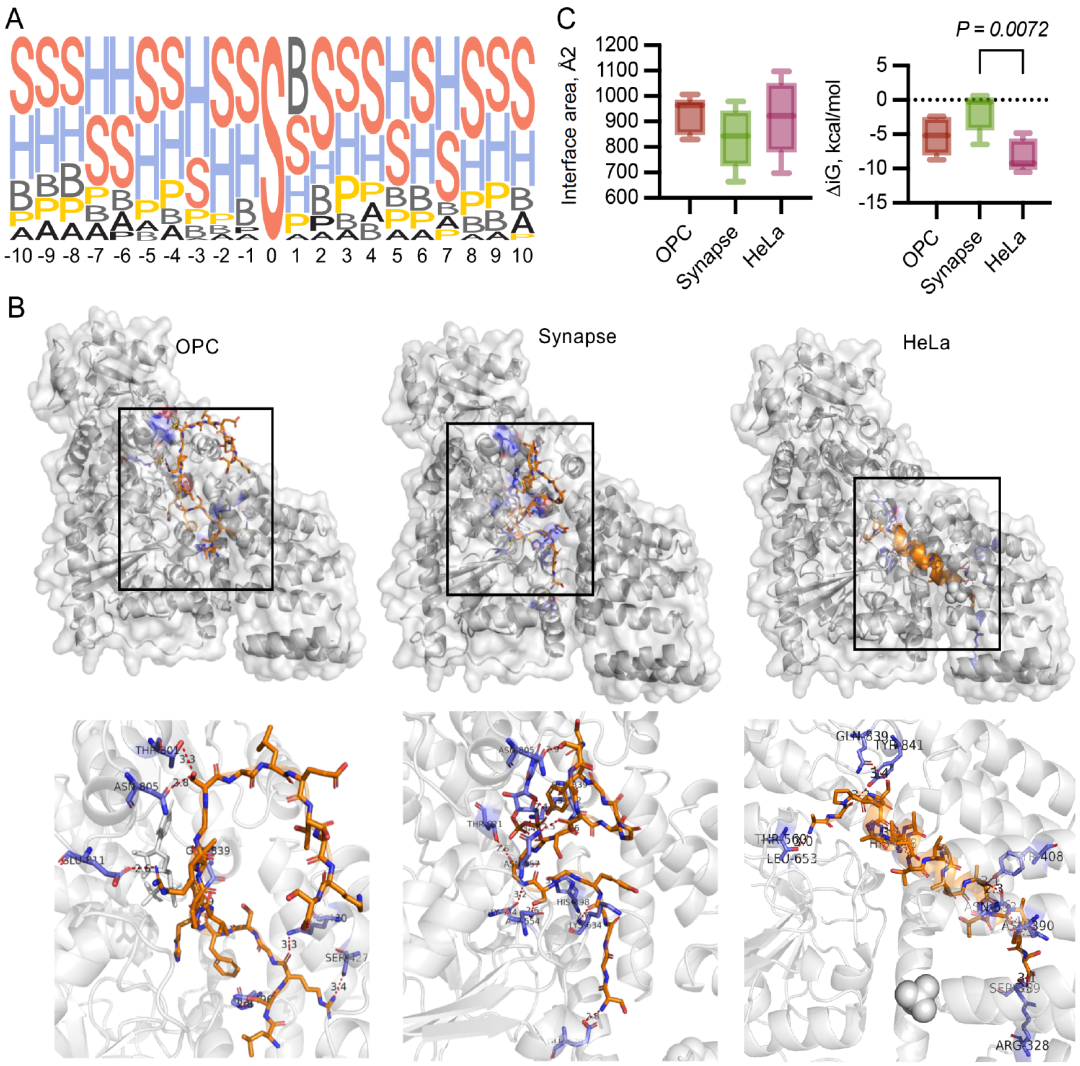


Figure 5. Chemical properties and OGT interactions of OPC O-GlcNAcylation motifs (A) Analysis of the chemical properties of amino acids surrounding O-GlcNAcylated sites in OPCs. (B) Molecular docking simulations showing the binding modes of representative O-GlcNAcylation peptides derived from OPCs, synapses, and HeLa cells with O-GlcNAc transferase (OGT). (C) Comparison of typical motifs, interface area, and binding free energy (ΔG) for OPCs, synapses, and HeLa cells from (B). *P* values were calculated using one-way ANOVA.

Figure S6A). We found that total O-GlcNAc levels in OPCs gradually increased from postnatal development to young adulthood and subsequently declined with advanced aging in both the cortex and the CC. Specifically, the MFI rose from 22.1 at P14 to 29.4 at 2 M in the cortex and from 19.3 to 28.0 in the CC, followed by a decrease to 18.8 and 13.0, respectively, at 12 M (Supplementary Figure S6B,C).

To explore whether key O-GlcNAcylated candidates contribute to age-related deficits in myelin repair capacity, we analyzed the expression dynamics of *Vim*, *Dbn1*, and *Flnb* in OPCs across the mouse lifespan. Transcriptomic data revealed that the expressions of *Vim*, *Dbn1*, and *Flnb* peaked during early development, specifically from P0 to P7, and declined thereafter (Figure 6A). In particular, *Vim* showed robust expression in neonatal OPCs followed by a decline during aging. *Dbn1* expression reached its maximum at P7 before decreasing, while *Flnb* exhibited high expression at P0 but remained low throughout later life stages.

To achieve greater cellular resolution, we interrogated these genes across functionally defined OPC subtypes using single-cell transcriptomic data spanning P30 to P720 [62]. These data reflected an age-dependent shift in OPC heterogeneity, characterized by a decrease in proliferative and differentiating populations alongside an expansion of the quiescent pool (Figure 6B,C). Within these subtypes, the expressions of *Vim*, *Dbn1*, and *Flnb* varied distinctly. UMAP analysis demonstrated that *Flnb* levels remained low across all ages. In contrast, *Vim* expression declined with age in transitioning OPCs but exhibited an increase in differentiating OLs (Figure 6D,E). Proteomic analysis confirmed that Vim and Dbn1 protein levels mirrored these transcriptional trends (Supplementary Figure S7A) [5]. Additionally, qRT-PCR showed that *Vim* mRNA was reduced in OLs, whereas *Dbn1* and *Flnb* were elevated in OLs (Supplementary Figure S7B). Specifically, *Vim* expression was found to be downregulated to approximately 0.2-fold in OLs compared to OPCs, while *Dbn1* levels increased to approximately 2.5-fold and *Flnb* showed a massive induction of over 120-fold

Table 2. OPC O-GlcNAcylated genes shared with both multiple sclerosis lesion proteome and multiple sclerosis snRNA-seq datasets

Gene name	Subcellular localization	Number of O-GlcNAcylated sites	Number of OPC-specific O-GlcNAcylated sites
Apc	Cytoplasm	1	1
Dbn1	Cytoplasm	2	2
Dmtn	Plasma membrane	1	0
Flnb	Cytoplasm	1	1
Htt	Cytoplasm	1	1
Irs2	Cytoplasm	1	0
Kif26b	Cytoplasm	1	1
Map6	Cytoplasm	1	0
Mtap	Cytoplasm	1	1
Mtss2	Cytoplasm	1	1
Pclo	Cell projection	6	0
Sgip1	Membrane	1	0
Trio	Cytoplasm	1	0
Tubb2b	Cytoplasm	1	1
Vim	Cytoplasm	2	2

relative to OPCs. Due to its dynamic regulation during differentiation, significant dysregulation in multiple sclerosis lesions, and high sensitivity to aging, we focused our further functional characterization on *Vim*.

O-GlcNAcylation of Vim is critical for OPC differentiation

Our proteomic analysis identified two O-GlcNAcylation sites on Vim, threonine 35 (T35) and threonine 63 (T63) (Supplementary Figure S8). To assess whether these modifications alter the intrinsic properties of Vim, we exogenously expressed HA (N-terminal)-tagged wild-type (Vim^{WT}) or an O-GlcNAc-deficient mutant ($Vim^{T35A\ T63A}$) in HEK293T cells. Immunostaining confirmed that both variants exhibited similar subcellular localization (Figure 7A,B).

To investigate the role of Vim O-GlcNAcylation in OPC differentiation, we utilized CRISPR-Cas9 technology to knock out *Vim* in the CG4 OPC line, followed by rescue with either Vim^{WT} or the O-GlcNAc-deficient mutant. Cells were selected with bleomycin for 3 days and subsequently induced to differentiate for an additional 3 days (Figure 7C). Knockout efficiency was confirmed by qRT-PCR, revealing an ~90% reduction in *Vim* mRNA (Figure 7D). Functional assays revealed that *Vim* KO impaired OPC differentiation, reducing the percentage of mature Mbp^+ cells to 8.48% compared to 21.68% in vector controls. While re-expression of Vim^{WT} rescued this differentiation defect (18.04% Mbp^+ cells), the O-GlcNAc-deficient $Vim^{T35A\ T63A}$ mutant exhibited a significant gain-of-function effect, further enhancing maturation to 28.59% Mbp^+ cells (Figure 7E,F). In addition, we performed qRT-PCR to evaluate the expressions of a panel of mature OL (*Mbp*, *Mog*, *Mag*, and *Plp1*) and OPC-related (*Pdgfrα* and *Olig2*) genes (Figure 7G). Consistent with the immunostaining data, the expression of all these OL genes was downregulated to less than 0.5-fold of the vector control levels in *Vim* KO cells compared to controls. This defect was rescued by Vim^{WT}, while $Vim^{T35A\ T63A}$ enhanced the rescue efficiency, increasing the expression of *Mbp* to approximately 2.0-fold, *Mog* to approximately 1.2-fold and *Plp1* to approximately 2.0-fold relative to the vector control. Regarding OPC-related genes, *Vim* KO led to aberrantly elevated *Olig2* and *Pdgfrα* levels to approximately 3.5-fold and 1.2-fold compared to the vector control, respectively, which were effectively restored to control levels by both Vim^{WT} and $Vim^{T35A\ T63A}$ rescues. Furthermore, we performed Ki67 and TUNEL staining (Supplementary Figure S9A,C). The results showed no significant differences in the proportion of $Ki67^+$ or $TUNEL^+$ cells between the vector control, *Vim* KO, and rescue groups (Supplementary Figure S9B,D).

Finally, to validate the identified O-GlcNAcylation sites of Vim, we performed immunoprecipitation assays. We expressed HA (C-terminal)- and Flag (N-terminal)-tagged Vim^{WT} or $Vim^{T35A\ T63A}$ in CG4 cells and enriched the proteins using anti-Flag beads. Western blot analysis revealed that, although not completely abolished, the O-GlcNAcylation level of the $Vim^{T35A\ T63A}$ mutant was reduced to approximately 50% compared to that of Vim^{WT} (Figure 8A–C). To rule out the possibility of protein degradation, we quantified the ratio of the C-terminal HA tag to the N-terminal Flag tag (Figure 8D). The HA/Flag ratio remained comparable between Vim^{WT} and mutant $Vim^{T35A\ T63A}$, indicating that the protein stability and full-length integrity were maintained. These results support that the observed reduction in the O-GlcNAc signal is largely due to the loss of the modification sites at T35 and T63.

Discussion

In this study, we profiled the O-GlcNAcome in neonatal mouse OPCs, identifying 165 O-GlcNAcylation sites across 118 proteins, predominantly nuclear and monosubstituted. Comparative analysis revealed 74 novel sites on 67 proteins, including 22 uniquely O-GlcNAcylated in OPCs, enriched in intrinsically disordered regions, linear interaction motifs, and pathways related to cytoskeletal organization and CNS development. Molecular docking simulations indicated intermediate binding affinities to Ogt. Integration with transcriptomic datasets from multiple sclerosis and aging contexts identified candidate proteins, including *Vim*. Functional validation confirmed Thr35 and Thr63 as O-GlcNAc sites on Vim, demonstrating that inhibiting this modification enhances OPC differentiation. This work establishes the first comprehensive O-GlcNAcome atlas for OPCs, providing an essential resource for elucidating myelination mechanisms and their dysregulation in demyelinating disorders.

Consistent with prior observations that Ogt preferentially targets IDRs [34,57], our data reinforce that O-GlcNAcylation is enriched in these conformationally flexible, non-folded domains (69.7% of sites). The flexible, non-folded structure of IDRs is essential for dynamic PPIs, molecular recognition, and cellular signaling regulation [58]. Because O-GlcNAcylation often occurs within these disordered regions, it is uniquely positioned to modulate the conformational plasticity of its targets, thereby regulating their biological functions. This structural modulation provides a biochemical basis for O-GlcNAcylation to act as a functional bridge between molecular signaling and complex neurodevelopmental processes [26,27,63]. LIPs, a functional subset of IDRs with intrinsic binding capability [64], were also heavily modified in our dataset (35.2%). Site-specific O-GlcNAcylation within LIPs is therefore likely to exert potent effects on rewiring protein interaction networks that govern OPC process extension, migration, and terminal differentiation.

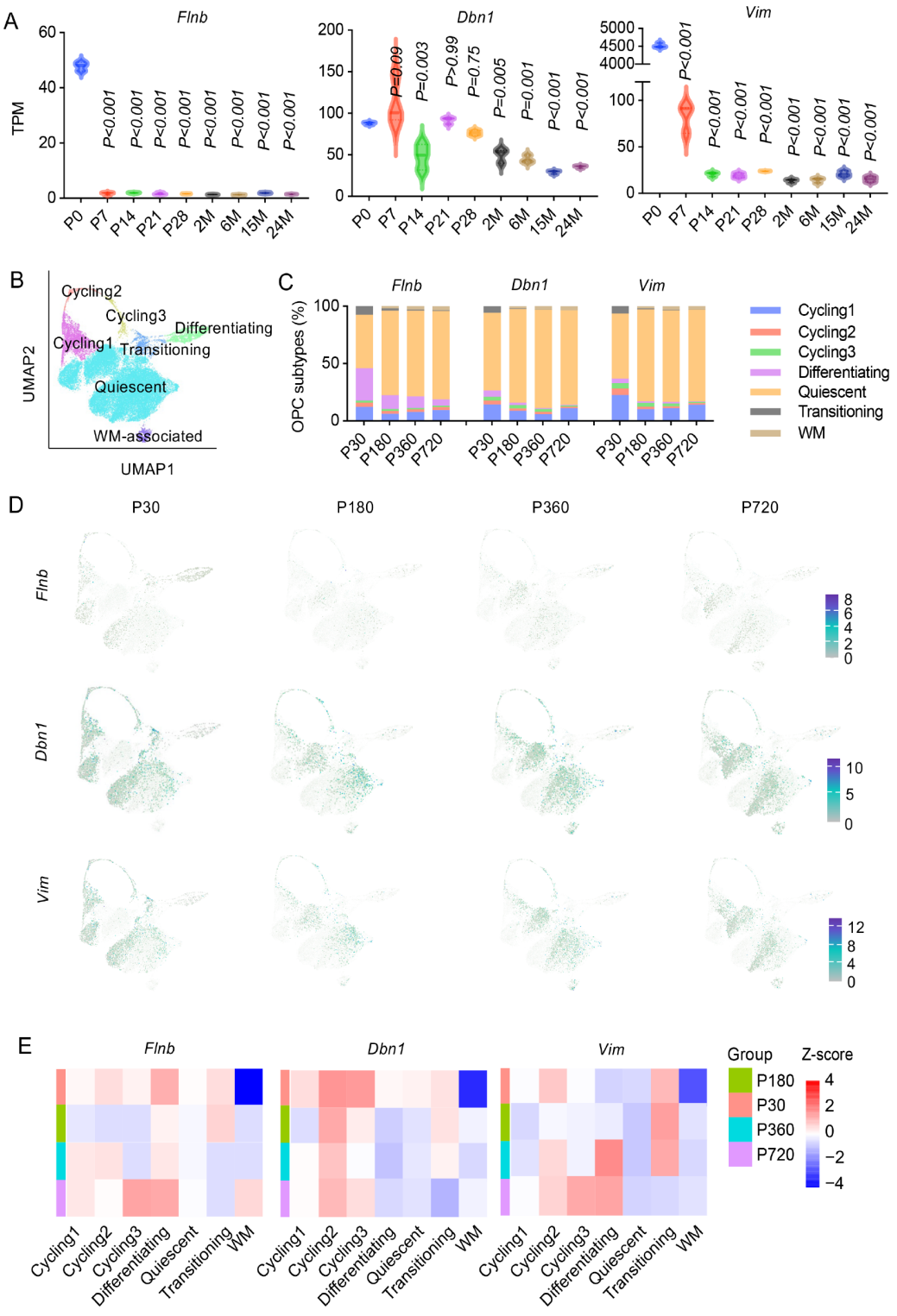


Figure 6. Expression dynamics of *Vim*, *Dbn1*, and *Flnb* in OPC subtypes during aging (A) Transcriptomic data (TPM) showing significant expression changes in *Flnb*, *Dbn1*, and *Vim* across postnatal ages (P0 to 24 M). (B) UMAP plot illustrating OPC subtypes (cycling, differentiating, quiescent, and transitioning) identified from single-cell transcriptomic data. (C) Stacked bar chart showing changes in the proportion of OPC subtypes at P30, P180, P360, and P720. (D,E) UMAP plots (D) and a heatmap (E) showing the expression levels of *Vim*, *Dbn1*, and *Flnb* across OPC subtypes at different ages. *P* values were calculated using one-way ANOVA.

Although global O-GlcNAcylation fluctuates with age, the underlying site-specific alterations are unresolved. Consequently, it is imperative for future studies to employ high-resolution, quantitative O-GlcNAcome profiling to capture the nuances of temporal

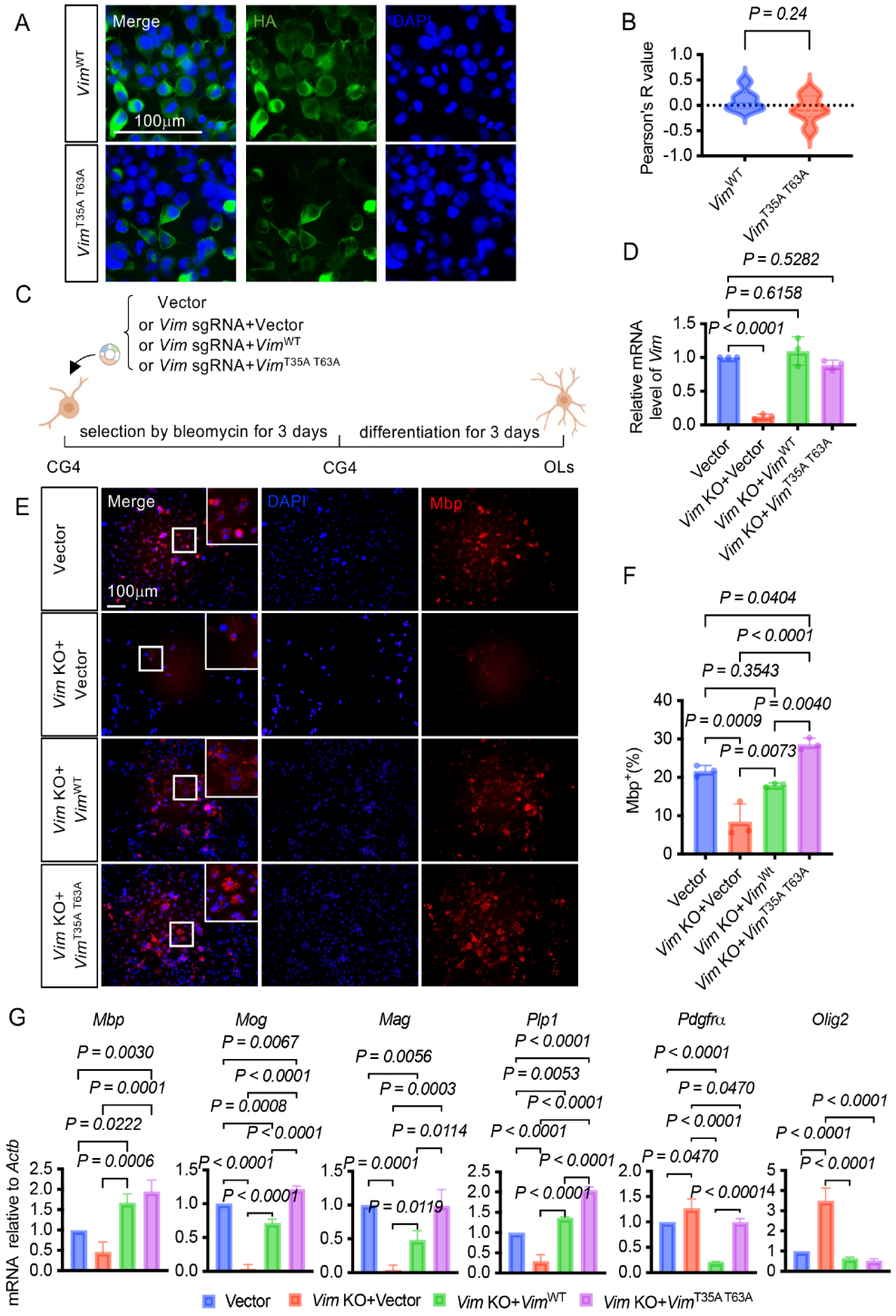


Figure 7. Functional validation of Vim O-GlcNAcylation in oligodendrocyte differentiation (A,B) Localization of HA-tagged Vim^{WT} and Vim$^{T35A\ T63A}$ in HEK293T cells. Scale bar: 100 μm. $n = 6$ independent biological experiments. (C) Schematic diagram of the experimental workflow. CG4 cells were transfected with constructs for *Vim* KO, Vim^{WT} rescue, or Vim$^{T35A\ T63A}$ rescue. Subsequently, the transfected cells were subjected to bleomycin selection for 3 days, during which OPC differentiation was simultaneously induced. (D) qRT-PCR analysis was used to evaluate the efficiency of *Vim* KO. The results showed that the expression level of *Vim* was reduced by approximately 90% in the *Vim* KO group compared with the control group. *P* values were calculated using two-tailed unpaired Student's *t* test. (E) Representative images of CG4 cells at the OL stage. Scale bar: 100 μm. n =3 independent biological experiments. (F) Statistical analysis of the positive rate of mature OLs (Mbp$^+$ cells) in CG4 cells. *P* values were calculated using one-way ANOVA. (G) qRT-PCR analysis was used to detect the mRNA expression levels of OL maturation-related genes (*Mbp*, *Mog*, *Mag*, and *Plp1*) and OPC-related genes (*Pdgfrα* and *Olig2*). *P* values were calculated using one-way ANOVA. n = 3 independent biological experiments.

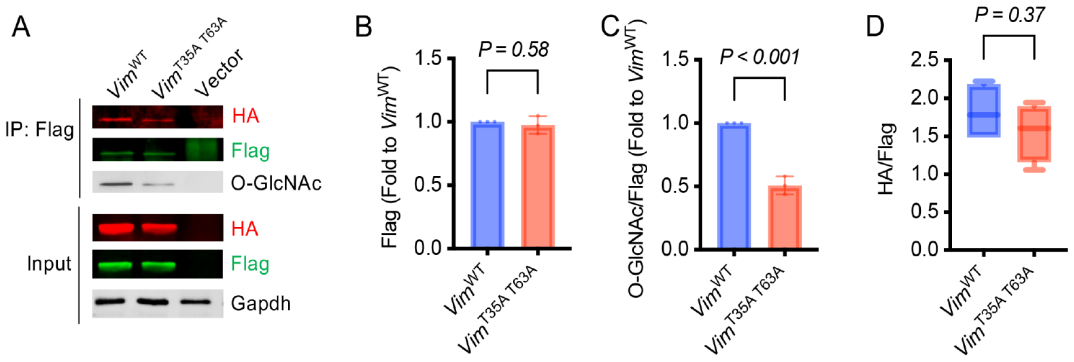


Figure 8. Analysis of Flag-HA-tagged Vim O-GlcNAcylation validation (A) Representative results of IP experiments comparing O-GlcNAcylation levels between Vim^{WT} and $Vim^{T35A\ T63A}$ and western blot analysis of Flag-HA-tagged Vim^{WT} and $Vim^{T35A\ T63A}$. Samples were collected from CG4. (B–D) Statistical analysis of the relative Flag levels (B), O-GlcNAc levels normalized to Flag (C) and HA normalized to Flag (D). $n = 3$ independent biological experiments. *P* values were calculated using two-tailed unpaired Student's *t* test.

differentiation. Currently, the technical challenges in the direct detection of Vim O-GlcNAcylation in mature OLs preclude a precise stoichiometric comparison across developmental stages. Our observation of increased Mbp^+ cell density likely reflects a shift in lineage commitment, suggesting potential alterations in the efficiency of oligodendrogenesis. Further mechanistic investigations should prioritize the identification of additional molecular candidates and the functional crosstalk between PTMs, particularly the O-GlcNAcylation-phosphorylation axis. These endeavors hold the potential to reveal novel therapeutic targets for alleviating differentiation arrest and fostering remyelination in demyelinating pathologies.

Supplementary Data

Supplementary data are available at *Acta Biochimica et Biophysica Sinica* online.

Data Availability

The O-GlcNAcome data have been deposited in PRIDE (Project PXD043506, https://www.ebi.ac.uk/pride/). Transcriptomic data about mouse OPCs across the lifespan have been deposited in the Sequence Read Archive (SRA, https://www.ncbi.nlm.nih.gov/) under SUB15247167. All other original data can be accessed upon reasonable request from the corresponding authors.

Acknowledgement

We thank Mingjie Chen (Shanghai NewCore Biotechnology Co., Ltd., Shanghai, China) for providing data analysis and visualization support.

Author Contributions

M.Z. designed research; X.J., P.L., Y.S., C.Z., and K.Y. performed research; X.J. analyzed data; M.Z., X.J., C.Z, and P.L. wrote the paper. All authors have read and given their approval for the final version of the manuscript.

Funding

This work was supported by the grant from the National Natural Science Foundation of China (No. 32370853).

Conflict of Interest

The authors declare that they have no conflict of interest.

References

1. Moura DMS, Brennan EJ, Brock R, Cocas LA. Neuron to oligodendrocyte precursor cell synapses: protagonists in oligodendrocyte development and myelination, and targets for therapeutics. *Front Neurosci* 2021, 15: 779125
2. Bradl M, Lassmann H. Oligodendrocytes: biology and pathology. *Acta Neuropathol* 2010, 119: 37–53
3. Clayton BLL, Tesar PJ. Oligodendrocyte progenitor cell fate and function in development and disease. *Curr Opin Cell Biol* 2021, 73: 35–40
4. Duncan GJ, Simkins TJ, Emery B. Neuron-oligodendrocyte interactions in the structure and integrity of axons. *Front Cell Dev Biol* 2021, 9: 653101
5. de la Fuente AG, Queiroz RML, Ghosh T, McMurran CE, Cubillos JF, Bergles DE, Fitzgerald DC, *et al.* Changes in the oligodendrocyte progenitor cell proteome with ageing. *Mol Cell Proteomics* 2020, 19: 1281–1302
6. Xiao Y, Czopka T. Myelination-independent functions of oligodendrocyte precursor cells in health and disease. *Nat Neurosci* 2023, 26: 1663–1669
7. Akay LA, Effenberger AH, Tsai LH. Cell of all trades: oligodendrocyte precursor cells in synaptic, vascular, and immune function. *Genes Dev* 2021, 35: 180–198
8. Nishiyama A, Shimizu T, Sherafat A, Richardson WD. Life-long oligodendrocyte development and plasticity. *Semin Cell Dev Biol* 2021, 116: 25–37
9. Elbaz B, Popko B. Molecular control of oligodendrocyte development. *Trends Neuroscis* 2019, 42: 263–277
10. Goldman SA, Kuypers NJ. How to make an oligodendrocyte. *Development* 2015, 142: 3983–3995
11. Caprariello AV, Batt CE, Zippe I, Romito-DiGiacomo RR, Karl M, Miller RH. Apoptosis of oligodendrocytes during early development delays myelination and impairs subsequent responses to demyelination. *J Neurosci* 2015, 35: 14031–14041
12. Tepavčević V, Lubetzki C. Oligodendrocyte progenitor cell recruitment and remyelination in multiple sclerosis: the more, the merrier? *Brain* 2022, 145: 4178–4192
13. Wang Q, Huang T, Zheng Z, Su Y, Wu Z, Zeng C, Yu G, *et al.* Oligodendroglial precursor cells modulate immune response and early demyelination in a murine model of multiple sclerosis. *Sci Transl Med* 2025, 17: eadn9980
14. Melchor GS, Khan T, Reger JF, Huang JK. Remyelination pharmacotherapy investigations highlight diverse mechanisms underlying multiple sclerosis progression. *ACS Pharmacol Transl Sci* 2019, 2: 372–386
15. Wolswijk G. Oligodendrocyte precursor cells in the demyelinated multiple

sclerosis spinal cord. *Brain* 2002, 125: 338–349
16. Dimovasili C, Fair AE, Garza IR, Batterman KV, Mortazavi F, Moore TL, Rosene DL. Aging compromises oligodendrocyte precursor cell maturation and efficient remyelination in the monkey brain. *GeroScience* 2023, 45: 249–264
17. Wang F, Ren SY, Chen JF, Liu K, Li RX, Li ZF, Hu B, *et al.* Myelin degeneration and diminished myelin renewal contribute to age-related deficits in memory. *Nat Neurosci* 2020, 23: 481–486
18. Spaas J, van Veggel L, Schepers M, Tiane A, van Horssen J, Wilson Iii DM, Moya PR, *et al.* Oxidative stress and impaired oligodendrocyte precursor cell differentiation in neurological disorders. *Cell Mol Life Sci* 2021, 78: 4615–4637
19. Morales MM, Pratt MR. The post-translational modification O-GlcNAc is a sensor and regulator of metabolism. *Open Biol* 2024, 14: 240209
20. Bond MR, Hanover JA. *O*- GlcNAc cycling: a link between metabolism and chronic disease. *Annu Rev Nutr* 2013, 33: 205–229
21. Ruan HB, Singh JP, Li MD, Wu J, Yang X. Cracking the O-GlcNAc code in metabolism. *Trends Endocrinol Metab* 2013, 24: 301–309
22. Shi RR, He TQ, Lin MS, Xu J, Gu JH, Xu H. O-GlcNAcylation in ischemic diseases. *Front Pharmacol* 2024, 15: 1377235
23. Yang X, Qian K. Protein O-GlcNAcylation: emerging mechanisms and functions. *Nat Rev Mol Cell Biol* 2017, 18: 452–465
24. Cheng SS, Mody AC, Woo CM. Opportunities for therapeutic modulation of O-GlcNAc. *Chem Rev* 2024, 124: 12918–13019
25. Cheng J, Zhao Z, Chen L, Li Y, Du R, Wu Y, Zhu Q, *et al.* Loss of O-GlcNAcylation on MeCP2 at threonine 203 leads to neurodevelopmental disorders. *Neurosci Bull* 2022, 38: 113–134
26. Chen L, Li Y, Song Z, Xue S, Liu F, Chang X, Wu Y, *et al.* O-GlcNAcylation promotes cerebellum development and medulloblastoma oncogenesis via SHH signaling. *Proc Natl Acad Sci USA* 2022, 119: e2202821119
27. Chen L, Jiang H, Licinio J, Wu H. Brain O-GlcNAcylation: bridging physiological functions, disease mechanisms, and therapeutic applications. *Mol Psychiatry* 2025, 30: 2754–2772
28. Zhang L, Bai W, Peng Y, Lin Y, Tian M. Role of O-GlcNAcylation in central nervous system development and injuries: a systematic review. *Mol Neurobiol* 2024, 61: 7075–7091
29. Lee BE, Suh PG, Kim JI. O-GlcNAcylation in health and neurodegenerative diseases. *Exp Mol Med* 2021, 53: 1674–1682
30. Pravata VM, Omelková M, Stavridis MP, Desbiens CM, Stephen HM, Lefeber DJ, Gecz J, *et al.* An intellectual disability syndrome with single-nucleotide variants in O-GlcNAc transferase. *Eur J Hum Genet* 2020, 28: 706–714
31. Brandt AU, Sy M, Bellmann-Strobl J, Newton BL, Pawling J, Zimmermann HG, Yu Z, *et al.* Association of a marker of *N*-acetylglucosamine with progressive multiple Sclerosis and neurodegeneration. *JAMA Neurol* 2021, 78: 842
32. Sy M, Brandt AU, Lee SU, Newton BL, Pawling J, Golzar A, Rahman AMA, *et al.* N-acetylglucosamine drives myelination by triggering oligodendrocyte precursor cell differentiation. *J Biol Chem* 2020, 295: 17413–17424
33. Zhang S, Tian Y, Wang Y, Wei F, Zhou H, Wen L. A reversible chemoenzymatic labeling strategy for profiling of protein O-glucosylation. *Angew Chem Int Ed* 2025, 64: e202513638
34. Trinidad JC, Barkan DT, Gulledge BF, Thalhammer A, Sali A, Schoepfer R, Burlingame AL. Global identification and characterization of both O-GlcNAcylation and phosphorylation at the murine synapse. *Mol Cell Proteomics* 2012, 11: 215–229
35. Qin K, Zhu Y, Qin W, Gao J, Shao X, Wang Y, Zhou W, *et al.* Quantitative profiling of protein O-GlcNAcylation sites by an isotope-tagged cleavable linker. *ACS Chem Biol* 2018, 13: 1983–1989
36. Wang S, Yang F, Petyuk VA, Shukla AK, Monroe ME, Gritsenko MA, Rodland KD, *et al.* Quantitative proteomics identifies altered O-GlcNAcylation of structural, synaptic and memory-associated proteins in Alzheimer's disease. *J Pathol* 2017, 243: 78–88
37. Hao Y, Li X, Qin K, Shi Y, He Y, Zhang C, Cheng B, *et al.* Chemoproteomic and transcriptomic analysis reveals that O-GlcNAc regulates mouse embryonic stem cell fate through the pluripotency network. *Angew Chem Int Ed* 2023, 62: e202300500
38. Ma J, Li Y, Hou C, Wu C. O-GlcNAcAtlas: a database of experimentally identified O-GlcNAc sites and proteins. *Glycobiology* 2021, 31: 719–723
39. Malard F, Massman L, Campagne S, Olivier-Van Stichelen S. The O-GlcNAc database: introducing new features and tools developed from community feedback. *Anal Bioanal Chem* 2025, 417: 879–884
40. Concordet JP, Haeussler M. CRISPOR: intuitive guide selection for CRISPR/Cas9 genome editing experiments and screens. *Nucleic Acids Res* 2018, 46: W242–W245
41. Huang DW, Sherman BT, Tan Q, Collins JR, Alvord WG, Roayaei J, Stephens R, *et al.* The DAVID gene functional classification tool: a novel biological module-centric algorithm to functionally analyze large gene lists. *Genome Biol* 2007, 8: R183
42. Tang D, Chen M, Huang X, Zhang G, Zeng L, Zhang G, Wu S, *et al.* SRplot: a free online platform for data visualization and graphing. *PLoS One* 2023, 18: e0294236
43. Horton P, Park KJ, Obayashi T, Fujita N, Harada H, Adams-Collier CJ, Nakai K. WoLF PSORT: protein localization predictor. *Nucleic Acids Res* 2007, 35: W585–W587
44. Mu H, Chen J, Huang W, Huang G, Deng M, Hong S, Ai P, *et al.* OmicShare tools: a zero-code interactive online platform for biological data analysis and visualization. *iMeta* 2024, 3: e228
45. Piovesan D, Del Conte A, Mehdiabadi M, Aspromonte MC, Blum M, Tesei G, von Bülow S, *et al.* MOBIDB in 2025: integrating ensemble properties and function annotations for intrinsically disordered proteins. *Nucleic Acids Res* 2025, 53: D495–D503
46. Finn RD, Bateman A, Clements J, Coggill P, Eberhardt RY, Eddy SR, Heger A, *et al.* Pfam: the protein families database. *Nucleic Acids Res* 2014, 42: D222–D230
47. Zhou P, Jin B, Li H, Huang SY. HPEPDOCK: a web server for blind peptide-protein docking based on a hierarchical algorithm. *Nucleic Acids Res* 2018, 46: W443–W450
48. Berman HM. The protein data bank. *Nucleic Acids Res* 2000, 28: 235–242
49. Lazarus MB, Jiang J, Gloster TM, Zandberg WF, Whitworth GE, Vocadlo DJ, Walker S. Structural snapshots of the reaction coordinate for O-GlcNAc transferase. *Nat Chem Biol* 2012, 8: 966–968
50. Richter-Landsberg C. The oligodendroglia cytoskeleton in health and disease. *J Neurosci Res* 2000, 59: 11–18
51. Biswas S, Kalil K. The microtubule-associated protein tau mediates the organization of microtubules and their dynamic exploration of actin-rich lamellipodia and filopodia of cortical growth cones. *J Neurosci* 2018, 38: 291–307
52. Ege N, Dowbaj AM, Jiang M, Howell M, Hooper S, Foster C, Jenkins RP, *et al.* Quantitative analysis reveals that actin and src-family kinases regulate nuclear YAP1 and its export. *Cell Syst* 2018, 6: 692–708.e13
53. Gohla A, Bokoch GM. 14-3-3 regulates actin dynamics by stabilizing phosphorylated cofilin. *Curr Biol* 2002, 12: 1704–1710
54. Greco TM, Secker C, Silva Ramos E, Federspiel JD, Liu JP, Perez AM, Al-Ramahi I, *et al.* Dynamics of huntingtin protein interactions in the striatum identifies candidate modifiers of Huntington disease. *Cell Syst* 2022, 13: 304–320.e5
55. Holliday GL, Mitchell JBO, Thornton JM. Understanding the functional

roles of amino acid residues in enzyme catalysis. *J Mol Biol* 2009, 390: 560–577
56. Li X, Keskin O, Ma B, Nussinov R, Liang J. Protein–protein interactions: hot spots and structurally conserved residues often locate in complemented pockets that pre-organized in the unbound states: implications for docking. *J Mol Biol* 2004, 344: 781–795
57. Chong PA, Nosella ML, Vanama M, Ruiz-Arduengo R, Forman-Kay JD. Exploration of O-GlcNAc transferase glycosylation sites reveals a target sequence compositional bias. *J Biol Chem* 2023, 299: 104629
58. Holehouse AS, Kragelund BB. The molecular basis for cellular function of intrinsically disordered protein regions. *Nat Rev Mol Cell Biol* 2024, 25: 187–211
59. Moreira IS, Fernandes PA, Ramos MJ. Hot spots—a review of the protein–protein interface determinant amino-acid residues. *Proteins* 2007, 68: 803–812
60. Han MH, Hwang SI, Roy DB, Lundgren DH, Price JV, Ousman SS, Fernald GH, *et al.* Proteomic analysis of active multiple sclerosis lesions reveals therapeutic targets. *Nature* 2008, 451: 1076–1081
61. Jäkel S, Agirre E, Mendanha Falcão A, van Bruggen D, Lee KW, Knuesel I, Malhotra D, *et al.* Altered human oligodendrocyte heterogeneity in multiple sclerosis. *Nature* 2019, 566: 543–547
62. Heo D, Kim AA, Neumann B, Doze VN, Xu YKT, Mironova YA, Slosberg J, *et al.* Transcriptional profiles of mouse oligodendrocyte precursor cells across the lifespan. *Nat Aging* 2025, 5: 675–690
63. Liu F, Li S, Zhao X, Xue S, Li H, Yang G, Li Y, *et al.* O-GlcNAcylation is required for the survival of cerebellar purkinje cells by inhibiting ROS generation. *Antioxidants* 2023, 12: 806
64. Peng Z, Li Z, Meng Q, Zhao B, Kurgan L. CLIP: accurate prediction of disordered linear interacting peptides from protein sequences using co-evolutionary information. *Brief BioInf* 2023, 24: bbac502